| **Titre:** Title: | Mechanosynthesis of TaC-WC powders under environmental conditions and their consolidation via electric arc furnace |
|---|---|
| **Auteurs:** Authors: | Adriana Vázquez Pelayo, Teresa Garcia-Mendoza, Ignacio Becerril-Juarez, Erick A. Juarez-Arellano, Karina Mireles, & Miguel Avalos-Borja |
| **Date:** | 2024 |
| **Type:** | Article de revue / Article |
| **Référence:** Citation: | Vázquez Pelayo, A., Garcia-Mendoza, T., Becerril-Juarez, I., Juarez-Arellano, E. A., Mireles, K., & Avalos-Borja, M. (2024). Mechanosynthesis of TaC-WC powders under environmental conditions and their consolidation via electric arc furnace. Materials Research Express, 11(6), 065601 (17 pages). https://doi.org/10.1088/2053-1591/ad55b1 |

| **URL de PolyPublie:** PolyPublie URL: | https://publications.polymtl.ca/58695/ |
|---|---|
| **Version:** | Version officielle de l'éditeur / Published version Révisé par les pairs / Refereed |
| **Conditions d'utilisation:** Terms of Use: | CC BY |

## Document publié chez l'éditeur officiel
Document issued by the official publisher

| **Titre de la revue:** Journal Title: | Materials Research Express (vol. 11, no. 6) |
|---|---|
| **Maison d'édition:** Publisher: | IOP Publishing |
| **URL officiel:** Official URL: | https://doi.org/10.1088/2053-1591/ad55b1 |
| **Mention légale:** Legal notice: | Original content from this work may be used under the terms of the Creative Commons Attribution 4.0 licence (http://creativecommons.org/licenses/by/4.0). Any further distribution of this work must maintain attribution to the author(s) and the title of the work, journal citation and DOI. |

# Materials Research Express

**PAPER**

# Mechanosynthesis of TaC-WC powders under environmental conditions and their consolidation via electric arc furnace

A Vázquez-Pelayo[1] , T Garcia-Mendoza[2], I G Becerril-Juarez[1], E A Juarez-Arellano[3] , L K Mireles[4] and M Avalos-Borja[1]

[1] División de Materiales Avanzados, Instituto Potosino de Investigación Científica y Tecnológica, San Luis Potosí 78216, Mexico
[2] División de estudios de Posgrado, Universidad de Papaloapan, Tuxtepec 68301, Mexico
[3] Instituto de Química Aplicada, Universidad de Papaloapan, Tuxtepec 68301, Mexico
[4] Département de Génie mécanique, École Polytechnique Montréal, Montréal 6079, Canada

E-mail: miguel.avalos@ipicyt.edu.mx

## Abstract

In this study, tantalum carbide (TaC) was synthesized using an innovative approach that synergistically integrates mechanosynthesis and electric arc furnace processes. By employing high-energy ball-milling (HEBM) for 50 min under environmental conditions, TaC-WC powders were successfully synthesized, using a powder mixture of tantalum and carbon in a 1:1 stoichiometric ratio. This method yielded a composition of 72.5 wt% TaC and 27.5 wt% WC, with an average particle size of $0.7 \pm 0.3\ \mu$m. The use of an electric arc furnace led to the fabrication of a highly dense material with a relative density above 98%. Notably, WC derived from the mechanical milling material served as an effective sintering aid. x-ray photoelectron Spectroscopy (XPS) results indicated the formation of metal oxides on the surface of the sample, and despite the presence of these oxides, the density of the material remained uncompromised. Furthermore, x-ray diffraction (XRD) analysis after the electric arc furnace treatment demonstrated the preservation of the TaC and WC phases. Mechanical properties, including Vickers hardness, Young's modulus and fracture toughness were $22.8 \pm 0.5$ GPa under an applied load of 9.8 N, 539 GPa and 6.6 MPa m$^{1/2}$, respectively. The results underscore a novel and efficient synthesis route for TaC-WC with enhanced mechanical properties and high density, which are crucial aspects for applications in ultra-high temperature ceramics.

## 1. Introduction

Tantalum carbide (TaC) is an interesting compound among transition metal carbides (TMC) due to its properties, including high hardness (15–19 GPa), high melting point (above 3880 °C), resistance to chemical attack, high elastic modulus, chemical and thermal stability, and electrical conductivity [1–4]. TaC has the NaCl-type structure (B1, space group $Fm\overline{3}m$) and exhibits the peculiarity of tolerating significant deficiencies in carbon content without changing its structure type [5]. These characteristics make TaC a promising material for ultra-high temperature ceramics (UHTCs) with diverse applications in aerospace propulsion systems, rocket nozzles, hard coatings, cutting tools and catalyst support [6, 7].

TaC powders are commonly synthesized through a carburization reaction at 1700 °C, using carbon and tantalum oxide (Ta$_2$O$_5$) as starting materials [8]. Other techniques have been employed, including solid-phase combustion synthesis, sol–gel method, chemical vapor deposition, carbothermal reduction and self-propagating high temperature synthesis [9]. Li *et al* used a solid-state reaction process involving Ta$_2$O$_5$ and C$_3$N$_4$ at 1150 °C for 1 h [10]. Liu *et al* employed a combination of sol–gel method and spark plasma sintering (SPS) to obtain TaC powders. Tantalum pentachloride (TaCl$_5$) and phenolic resin were dissolved in ethanol at 80 °C. After 6 h, gels were formed and dried at 120 °C for 24 h. Subsequently, a pyrolysis method was carried out at 800 °C, followed by SPS with temperatures varying from 1400 °C–1600 °C [11]. Sevast'yanov *et al* synthesized

**Table 1.** Synthesis conditions of planetary ball milling.

| Ball mill type | Planetary |
|---|---|
| milling speed, rpm | 600 |
| milling time, min | 50 |
| vial capacity, ml | 80 |
| ball diameter, mm | 10 |
| number of balls | 15 |
| milling material | WC |
| ball to powder ratio | 115:1 |

tantalum monocarbide powders via carbothermic reduction using $Ta_2O_5$ and carbon as starting materials, at temperatures ranging from 850 to 1200 °C and pressures from $10^{-5}$ to $10^{-4}$ MPa [12]. We can observe that these methods involved different starting materials, high temperatures, and extended synthesis times, among other factors. Therefore, High-energy ball milling (HEBM) enables the synthesis of materials under environmental conditions [13]. Changes occur in morphology, grain and particle size, leading to improvements in the mechanical properties such as hardness, attributed to the Hall-Petch effect where hardness increases as grain size decreases [14, 15]. There are limited reports of TaC synthesis via HEBM; Garcia-Mendoza *et al* synthesized TaC using this method in 30 min [16]. Mechanosynthesis is commonly used as a mechanical treatment for commercial TaC powders to homogenize the materials and change the particle size [17]. Manotas-Albor *et al* sintered TaC nanodispersoids in a copper matrix; they employed mechanical milling under nitrogen atmosphere at different milling times (10, 20 and 30 h), followed by hot–extrusion [18]. Liu *et al* used mechanosynthesis for 4 h to homogenize TaC and $Si_3N_4$ powders. The resulting material was dried at 80 °C and then consolidated via SPS at 1700 °C under a constant pressure of 30 MPa [19].

TaC densification is a challenging process, due to the low self-diffusion coefficient ensuing from the covalent bond between carbon and tantalum. The techniques commonly used to consolidate TaC are SPS, hot pressing (HP) and high-pressure methods. Li *et al* achieved the sintering of TaC-SiC ceramics using SPS at 1600 °C under 30 MPa [20]. Zhang *et al* consolidated TaC via HP at temperatures ranging from 1900 to 2400 °C [21]. Sun *et al* used a high-pressure method to consolidate TaC at 1400 °C under a pressure of 5.5 GPa [22]. Additionally, various studies have indicated that the inclusion of materials such as $B_4C$, HfC, Si, SiC, $MoSi_2$, and WC, among others, improves the densification of the TaC [17, 23, 24]. The incorporation of WC during the HEBM process can yield notable benefits, as WC exhibits compelling characteristics, including high hardness, catalytic activity, high melting point and resistance to oxidation [25–27]. Kelly *et al* incorporate WC into TaC to prevent grain growth leading to a higher relative density and increased fracture strength [28].

Hence, there is a need for synthesis methods that enable the rapid production of TaC powders under environmental conditions, as well as straightforward and swift sintering techniques that concurrently enable us to obtain dense materials with desirable mechanical properties. The reduction of material manufacturing times, combined with obtaining products under environmental conditions, plays a crucial role in decreasing production costs. In the present work, TaC was synthesized by HEBM under environmental conditions in a few minutes of milling. Subsequently, the material was consolidated in an electric arc furnace to form dense pellets which are crucial for different applications, optimizing times and costs.

## 2. Materials and methods

### 2.1. Powder preparation and synthesis

Synthesis of tantalum carbide followed a previously reported methodology [13, 16]; in summary, tantalum carbide was prepared from a stoichiometric powder mixture of tantalum (Sigma-Aldrich, 99.9%) and carbon (graphite, Sigma-Aldrich, <20 $\mu$m) with a 1:1 molar ratio. The raw materials were placed in a mortar and mechanically treated with mortar and pestle until a finely homogenous powder was obtained. The high-energy ball milling process was conducted in a planetary ball-mill (Pulverisette 7 premium line, Fritsch). Cycles of 5 min milling and 10 min pauses were implemented to minimize overheating. The synthesis conditions are detailed in table 1.

### 2.2. TaC-WC consolidation via electric arc furnace

The powders obtained through HEBM were used to create pellets using a mechanical press with a cylindrical die. These pellets were consolidated with an electric arc furnace (Edmund Bühler Arc Melter MAM-1). Prior to the sintering process, several purging cycles were executed. The vacuum was established by introducing ultra-high

purity argon gas (UHP; 99.999%). These vacuum-argon cycles were repeated four times to ensure that the sintering process took place in an inert environment. Upon completion of the cycles, a titanium target (placed in a crucible separated from the samples) was melted to absorb any remaining oxygen. Once the titanium target had melted, an electric arc was initiated to melt the TaC-WC samples. The bulk density of TaC-WC was determined with the Archimedes method, and theoretical densities were calculated by the law of mixtures considering the phase composition of the powders. Relative density was quantified as the percentage fraction of the bulk density compared to the theoretical density.

### 2.3. Characterization of TaC-WC powders after HEBM

TaC evolution reaction was monitored by x-ray diffraction (XRD). XRD patterns were acquired using a Rigaku's Smartlab diffractometer (Rigaku Corp., Japan) at 40 kV and 44 mA employing Cu K$\alpha$ radiation ($\lambda = 1.5406$ Å). The examined $2\theta$-interval ranged from 20 to 90° with a 0.01° step size. Peaks were identified using PDF4+2022 database. To determine the weight percentage of crystalline phases present in the samples, Rietveld's refinement analysis method was applied. In addition, the Williamson–Hall method was employed to determine the particle size and microstrain of the material. Both Rietveld refinement and Williamson–Hall method were performed using the X'Pert High Score Plus© v 5.0 software [29].

Morphological and elemental analyses were conducted in a scanning electron microscope (SEM) FEI's Quanta 250 FEG SEM (Thermofisher Scientific Inc., USA), equipped with an energy-dispersive x-ray spectroscopy (EDS) detector. Samples were mounted on silicon substrates. Several regions of the sample were selected for the measurements.

A transmission electron microscope study was performed in a HR-TEM FEI's Tecnai F30 (Thermofisher Scientific Inc., USA) at 300 keV. Data analysis was carried out using Digital Micrograph® software. In addition, MacTempasX® software facilitated the simulation of diffraction patterns and HR-TEM [30].

The specific surface area was determined using the BET method ($N_2$ absorption at 77 K), employing a porosity measuring system BELSORP-mini surface area equipment. Preceding the analysis, the samples were degassed at 373 K in an inert atmosphere using nitrogen ($N_2$).

Differential scanning calorimetry (DSC) was employed to characterize the phase transition temperature, using a 250 Discovery instrument (TA Instruments®/Waters™, USA) with measurement conducted from room temperature (25 °C) to 450 °C at a heating rate of 10 °C min$^{-1}$ in an inert atmosphere ($N_2$).

### 2.4. Sample preparation and characterization after electric arc furnace treatment

Pellets obtained via electric arc furnace were mounted on an Epoxy resin polymerized using the Buehler's EpoThin™ (Epoxy resin 20–3442–032 and Epoxy hardener 20-3440-016). Subsequently, samples were polished to achieve a homogeneous surface, free of porosity and roughness.

X-ray photoelectron spectroscopy (XPS) was conducted with an ESCALAB QXi (Thermofisher Scientific Inc., USA), using monochromated Al K$\alpha$ x-rays ($h\nu = 1486.6$ eV) at a perpendicular take-off angle. Data analysis was carried out with the VG Avantage (Thermo Scientific™) software. Peak fitting considered the presence of C-C at 284.8 eV. To remove impurities from the surface sample, a sputtering with Ar gas was performed for 360 s with an energy of 2 keV.

Hardness was measured using a micro-Vickers Mitutoyo HM-220 testing machine (Mitutoyo corp., Japan), following ASTM Standard E384–17 [31]. Different loads were applied (0.49, 0.98, 2.94, 4.9 and 9.8 N) with a dwell time of 15 s. Five indentations per load were made to obtain the average hardness value and the standard deviation. Vickers hardness was calculated using the equation (1) by measuring the diagonal lengths printed by a pyramidal diamond indenter with a 136° angle between its lattices [32, 33].

$$Hv = \frac{(1854.4)\, F}{D^2} \tag{1}$$

Where $Hv$ is Vickers hardness (GPa), F is the applied force (g$_f$) and D is the printed diagonals average made by the indenter ($\mu$m) [33].

Nielsen formula (equation (2) was employed to estimate Young's modulus (*E*) [34].

$$E = E_0 \frac{(1 - P)^2}{1 + (\rho^{-1} - 1)P} \tag{2}$$

Where $E_0$, represents the Young's modulus of the fully dense material (537 GPa for TaC) [35], P denotes the vol% of the porosities, and $\rho$ is the Nielsen's shape factor ($\sim$0.4).

Antis formula (equation (3)) was used to determine the fracture toughness ($K_{1C}$), estimated by measuring the length of diagonal cracks originating at the corners of Vickers indentation under higher loads [36].
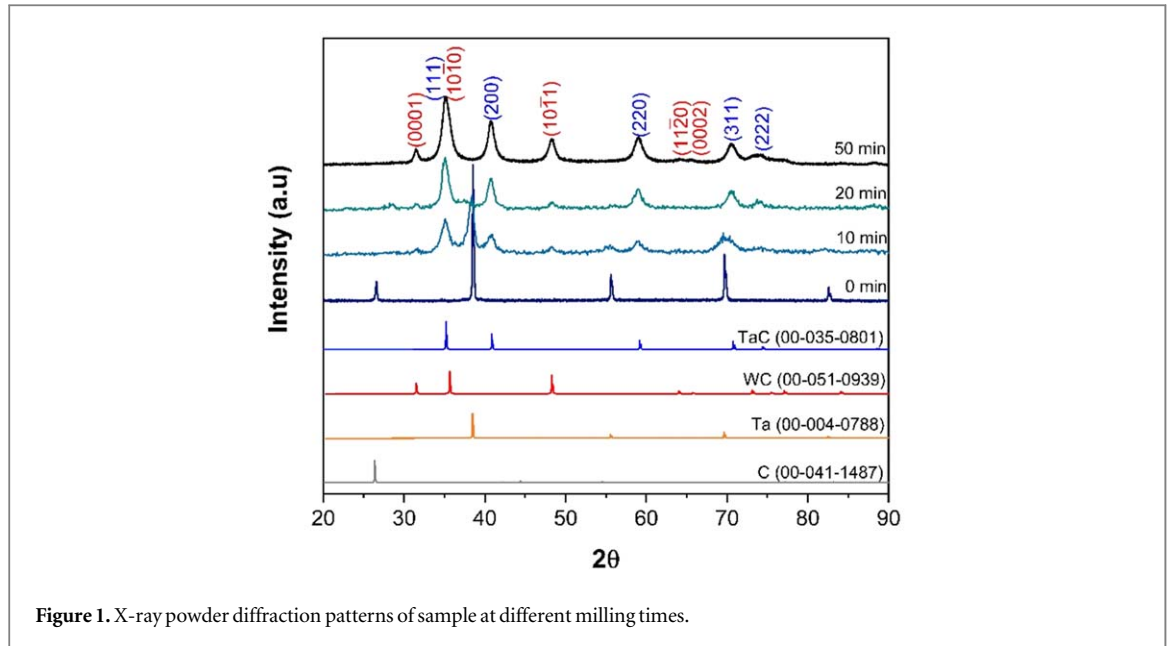
**Figure 1.** X-ray powder diffraction patterns of sample at different milling times.

$$K_{1C} = 0.016 \left( \frac{E}{H_v} \right)^{\frac{1}{2}} P c^{-\frac{3}{2}} \tag{3}$$

Where $P$ is the indentation load, $E$ is the Young Modulus, $H_v$ is the Vickers harness, and $c$ is the sum of crack length and half-length indentation diagonal.

SEM analysis was conducted using a FEI's Quanta 250 FEG SEM (Thermofisher Scientific Inc., USA) to observe and measure the crack length.

## 3. Results and discussion

### 3.1. TaC-WC powders characterization

Figure 1 shows powder diffraction patterns of the samples before and after HEBM process. The diffractograms were collected at milling times of 0, 10, 20 and 50 min.

Prior to the HEBM process at 0 min, the diffractogram reveals peaks from the raw materials, corresponding to Ta (space group $Im\bar{3}m$) and graphite (space group $P6_3/mmc$). The diffractograms show that the formation of TaC becomes discernible after 10 min of milling. TaC (space group $Fm\bar{3}m$) and WC (space group $P\bar{6}m2$), were both identified at this stage. WC presence is attributed to the materials constituting the milling vial and the balls. As the milling process progresses to 50 min, the full formation of TaC is observed. It is important to mention that despite the coexistence of WC milling material in the sample, no observable reaction between TaC and WC was detected.

Different studies have reported the use of commercially available TaC powders [20, 37, 38], typically synthesized under high-temperature or high-pressure conditions, requiring extended synthesis times [8, 11, 39]. In this study, TaC powders were synthesized through HEBM under environmental conditions. The initiation of material formation occurred at 10 min, while at 50 min no traces of the raw material were detected. Conducting the synthesis at ambient temperature and pressure within 50 min yields substantial energy savings, marking a notable advancement in the efficient production of TaC powders.

Crystalline phases in the 50-minute XRD experimental data were quantified using a Rietveld refinement. The results obtained are shown in figure 2. The sample contains 72.5 wt% TaC and 27.5 wt% WC. R-values from the refinement were 5.49 for $R_{exp}$, 5.61 for $R_p$ and 7.01 for $R_{wp}$. Due to the sample's composition, it will be referred to as TaC-WC. Lattice and Rietveld refinement parameters are presented in table 2.

In our previous work [16], we reported the TaC-WC lattice parameters at 30 min of milling. In the WC phase, a slight increase in the '*a*' and '*c*' parameters was observed. This phenomenon, noted in various studies, is attributed to the incorporation of impurities present in the raw materials during the synthesis process, as Cedillos-Barraza *et al* mentioned [17]. However, the lattice parameter values obtained through the Rietveld refinement align with the PDF4+ data base.

The crystalline size and microstrain for the sample obtained at 50 min of milling were calculated using the Williamson–Hall method. Figure 3 shows the graphs acquired for the two different phases. The size-strain plot
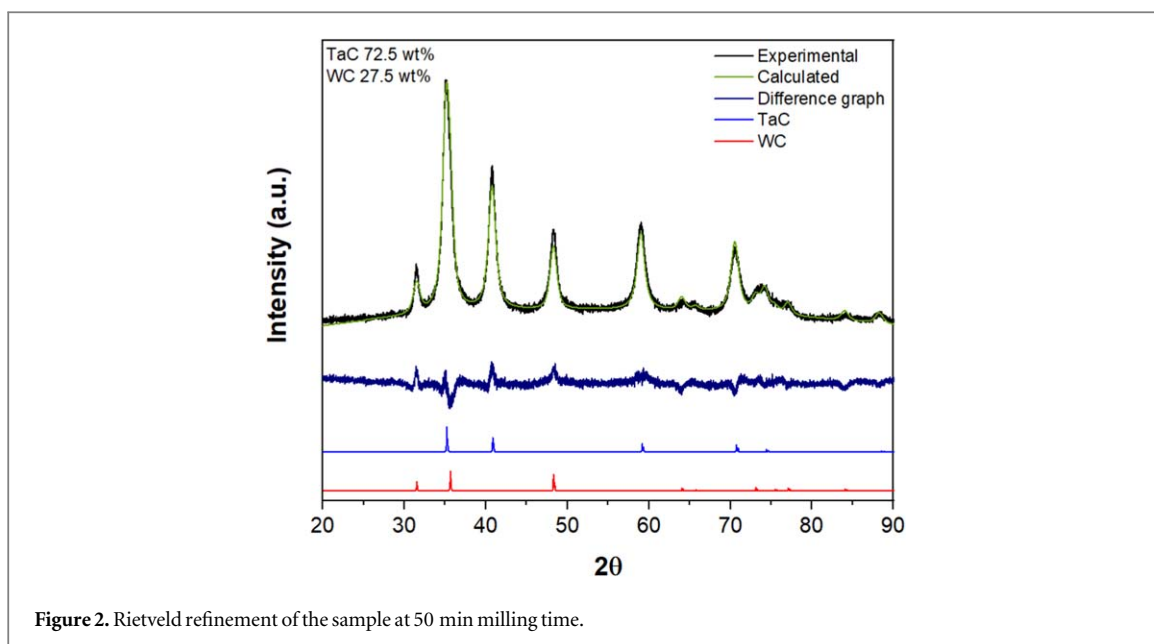
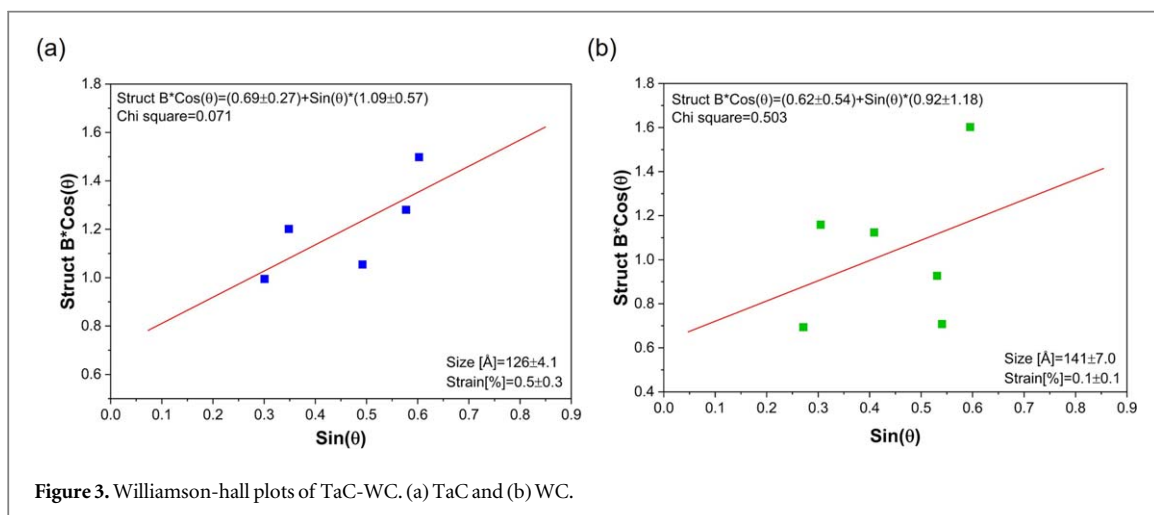**Figure 2.** Rietveld refinement of the sample at 50 min milling time.



**Figure 3.** Williamson-hall plots of TaC-WC. (a) TaC and (b) WC.

**Table 2.** Crystalline structure, lattice parameters, crystalline size and reliability factors from the Rietveld refinement of the TaC-WC powders after 50 min of milling.

|  | TaC | WC |
|---|---|---|
| Structure |  |  |
| Atoms | *Ta ; C* | *W ; C* |
| Space group | **Fm3̄m** | **P6̄m2** |
| Wykoff position | *4b ; 4a* | *1a ; 1d (z = 0.5)* |
| Occupation | *1:1* | *1:1* |
| Wt% | *72.5* | *27.5* |
| Lattice parameters |  |  |
| a/Å | *4.42* | *2.91* |
| b/Å | — | — |
| c/Å | — | *2.84* |
| V/Å³ | *86.91* | *20.85* |
| Reliability factors |  |  |
| $R_{exp}$ | *5.49* |  |
| $R_p$ | *5.61* |  |
| $R_{wp}$ | *7.01* |  |

**Figure 4.** SEM micrographs and EDS of the samples at 0 min of milling, (a) secondary electron image, (b) BSE image, (c) EDS spectra of blue area and (d) EDS spectra of orange area.
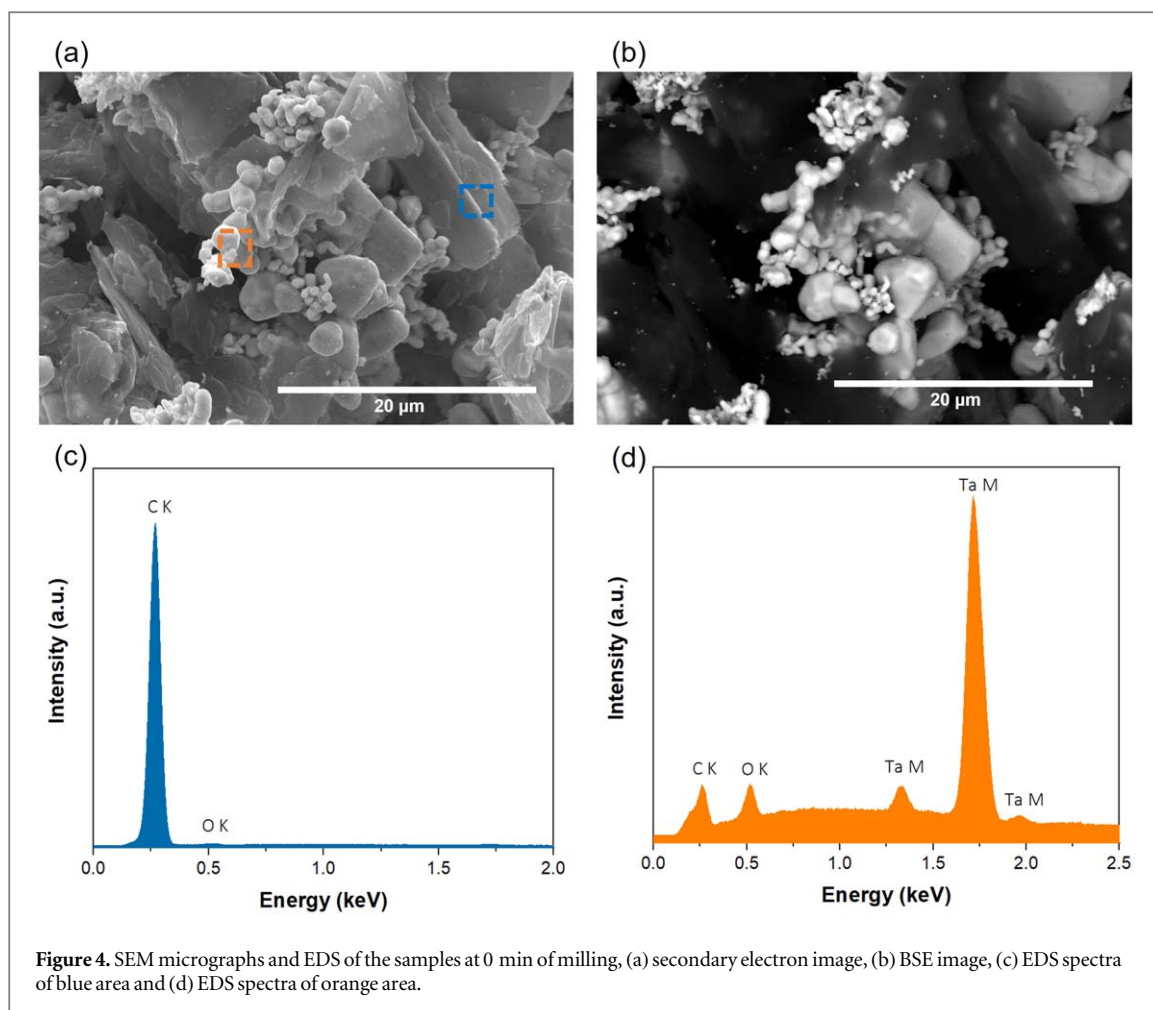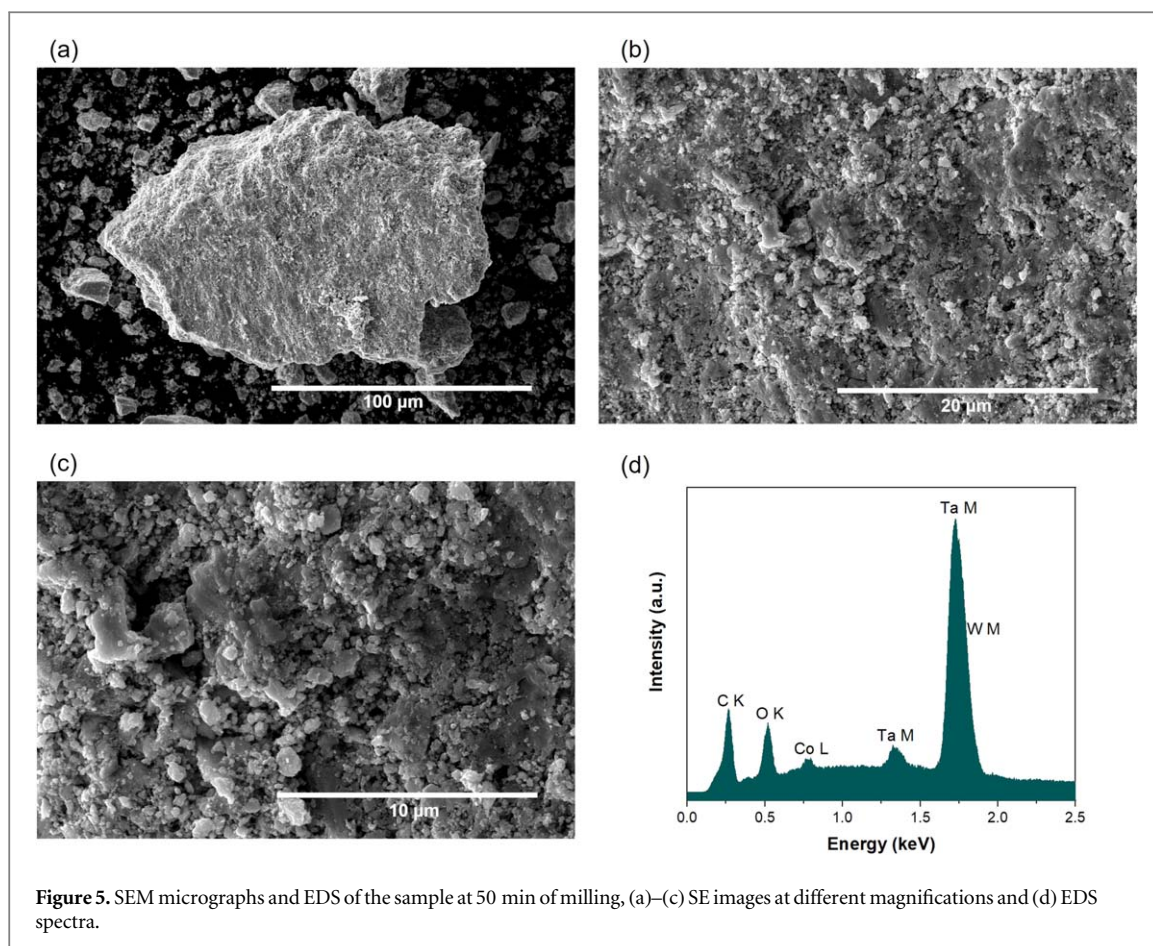
method is an approach that accounts for the XRD peak profile as a combination of Gaussian and Lorentzian functions. TaC exhibited an average crystallite size of $126 \pm 4.1$ Å, determined by the slope of the straight line, while the strain was $0.5 \pm 0.3\%$, calculated from the intercept (figure 3(a)). On the other hand, WC presented an average crystallite size of $141 \pm 7.0$ Å and a strain of $0.3 \pm 0.4\%$ (figure 3(b)). According to the findings of Al-Habib D S H *et al* [40], the crystallite size observed in the present work is smaller, a result that can be attributed to the HEBM process. This reduction in crystallite size may enhance mechanical properties of the material due to the Hall-Petch effect [41].

Morphology through the synthesis process was analyzed by SEM at 0 and 50 min. Figure 4(a) shows the micrographs obtained at 0 min, revealing samples composed of agglomerates of semi-spherical particles of different sizes, alongside thin-sheets. In figure 4(b), the micrograph obtained by back scattered electrons (BSE) highlights a contrast between these two morphologies.

It was identified that semi-spherical particles correspond to Ta, while the thin-sheets correspond to graphite. This analysis was corroborated by EDS, as shown in figures 4(c) and (d), conducted in two different areas marked with blue and orange squares in figure 4(a).

Micrographs of the samples at 50-min of HEBM are presented in figure 5. The samples consist of agglomerates with a size of $0.7 \pm 0.3$ $\mu$m (figure 5(a)). Notably, there is no evidence of graphite, aligning with XRD results, since at 50 min of mechanosynthesis the graphite was amorphized and incorporated into the sample. At higher magnification, it is evident that the agglomerates predominantly consist of irregular particles of different sizes (figures 5(b) and (c)). EDS spectra (figure 5(d)) indicates that the particles are primarily composed of tantalum (Ta) and carbon (C), whilst the signals of tungsten (W) and cobalt (Co) reveal the presence of WC-Co, used as milling material (vials and balls). Furthermore, the presence of oxygen (O) could suggest oxidation on the TaC-WC surface. The particle size obtained via HEBM is similar to, or smaller than the particle sizes of the commercial powders used in various studies [42, 43].

Sample microstructure was also analyzed by TEM, and micrographs are shown in figure 6. The low magnification bright field (BF) image (figure 6(a)) shows particles with semi-spherical morphology with different sizes. These results are consistent with SEM analysis. Furthermore, the crystallite sizes align with those obtained through Rietveld refinement.

**Figure 5.** SEM micrographs and EDS of the sample at 50 min of milling, (a)–(c) SE images at different magnifications and (d) EDS spectra.

To complement the structure analysis, a selected area diffraction pattern (SAED) was obtained from the particles in figure 6(a). The diffraction pattern (DP) is characteristic of a polycrystalline material (figure 6(b)) and reveals interplanar distances of 2.5, 2.2, 1.5, 1.3 and 1.1 Å, corresponding to the planes (111), (200), (220), (311) and (400), respectively.
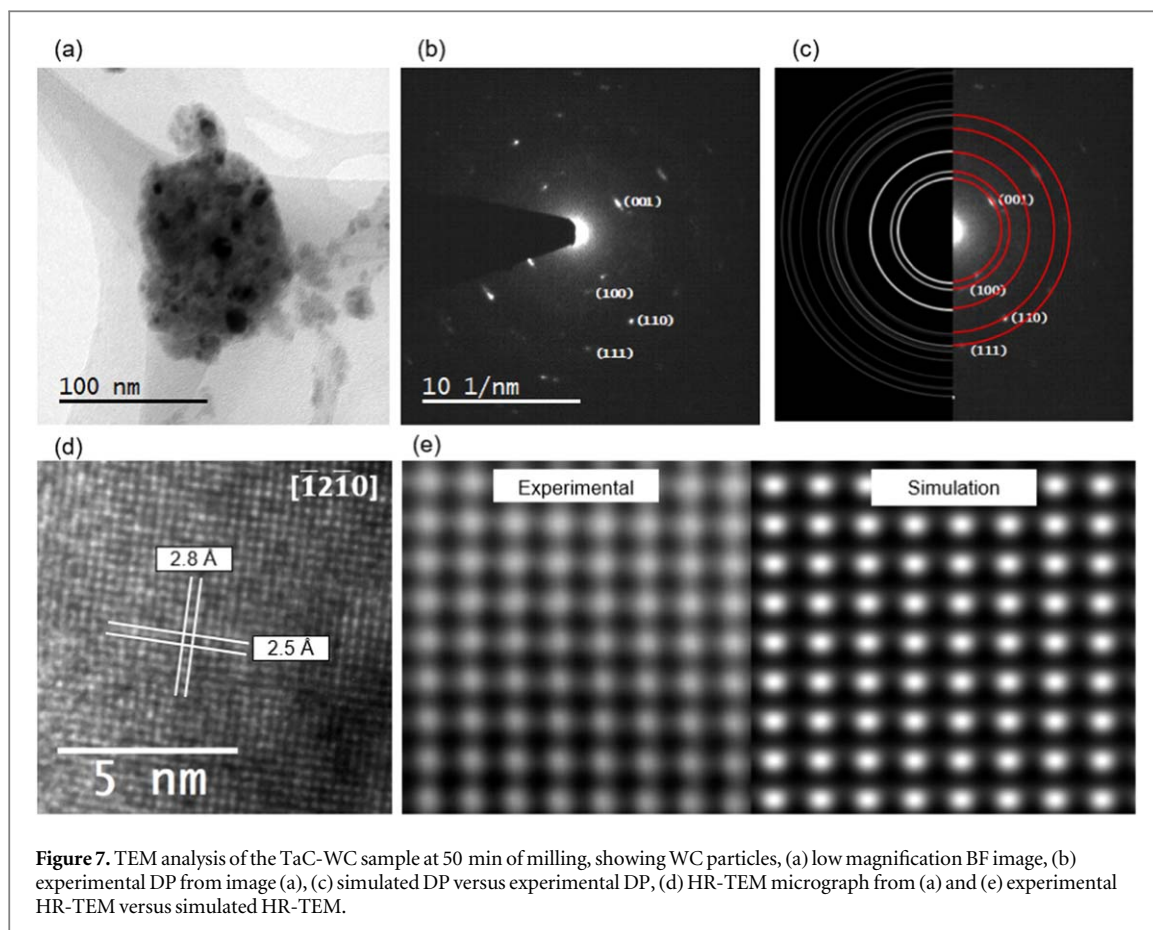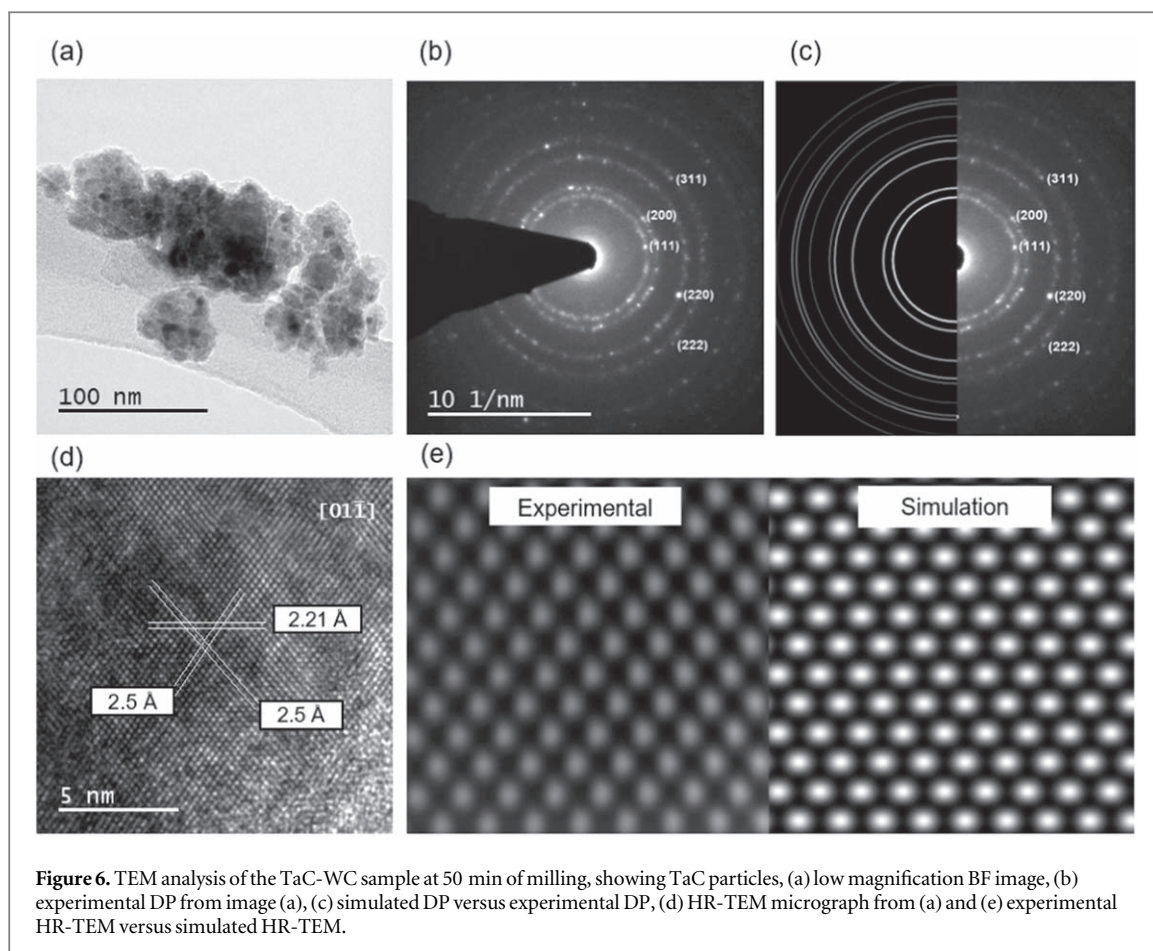
The analysis allowed the identification of TaC particles with a space group of $Fm\overline{3}m$, correlating with the XRD analysis. To confirm the information obtained, a DP simulation was performed. The DP-simulated images align with the experimental DP images, as seen in figure 6(c). HR-TEM was performed, and the information obtained is shown in figure 6(d). According to the analysis, interplanar distances of 2.5 and 2.2 Å corresponding to the (111) and (200) TaC planes were found.
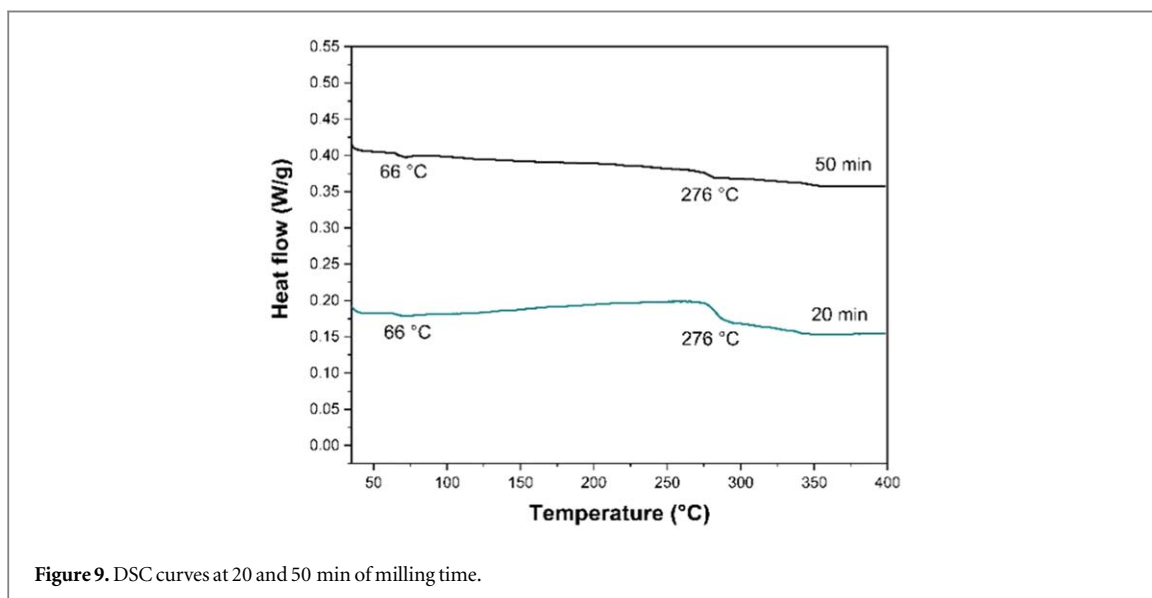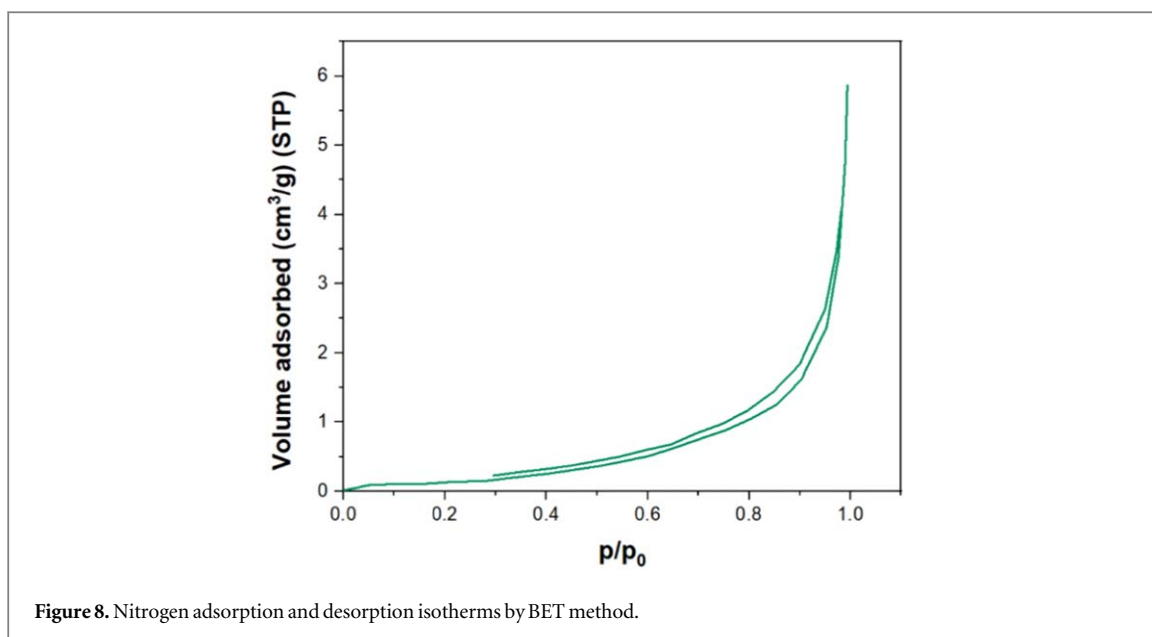
Figure 6(e) shows the HR-TEM simulation obtained in comparison to the experimental micrograph seen from the $[01\overline{1}]$ zone axis. The simulation is well-correlated with the experimental image.

Some other areas were analyzed. The low magnification BF micrograph is presented in figure 7(a) and shows particles with semi-spherical morphology of varying sizes. The DP was obtained from figure 7(a) and corresponds to a polycrystalline material (figure 7(b)). The indexing of the DP was carried out, and the analysis revealed the presence of interplanar distances of 2.8, 2.5, 1.4 and 1.2 Å corresponding to the planes (001), (100), (110) and (111), respectively.

Based on the results, it was concluded that the particles correspond to WC (space group $P\overline{6}m2$ (figure 7(b)). The DP simulation aligns with the experimental one, as can be seen in figure 7(c). HR-TEM was performed, and the information obtained is presented in figure 7(d). According to the analysis, interplanar distances of 2.8 Å and 2.5 Å corresponding to the plane (001) and (100) of WC were found, observed from the $[\overline{1}2\overline{1}0]$ zone axis. The HR-TEM simulation versus experimental micrograph is shown in figure 7(e). The simulation is well-correlated with the experimental image, corroborating the analysis.

Figure 8 shows the adsorption/desorption isotherms of the TaC-WC powders. The samples exhibit a type II isotherm with a type H3 loop according to the International Union of Pure and Applied Chemistry (IUPAC) classification [44]. This type of isotherm is characteristic of nonporous or macroporous materials. However, the desorption isotherm follows a different trajectory, leading to the formation of hysteresis. This hysteresis limits the region of the multilayer and is therefore considered not to be completely reversible. According to Sing *et al* [45], this type of isotherm is observed in materials that contain pores with cleft-like shapes or aggregates of particles with plate-like shapes. BET analysis showed that the samples have a BET surface area of 0.47 m$^2$/g,

**Figure 6.** TEM analysis of the TaC-WC sample at 50 min of milling, showing TaC particles, (a) low magnification BF image, (b) experimental DP from image (a), (c) simulated DP versus experimental DP, (d) HR-TEM micrograph from (a) and (e) experimental HR-TEM versus simulated HR-TEM.



**Figure 7.** TEM analysis of the TaC-WC sample at 50 min of milling, showing WC particles, (a) low magnification BF image, (b) experimental DP from image (a), (c) simulated DP versus experimental DP, (d) HR-TEM micrograph from (a) and (e) experimental HR-TEM versus simulated HR-TEM.

**Figure 8.** Nitrogen adsorption and desorption isotherms by BET method.



**Figure 9.** DSC curves at 20 and 50 min of milling time.

whilst the porous diameter and total volume porous ($p/p_0 = 0.990$) were 66.16 nm and 0.0077 $cm^3/g$, respectively.

Figure 9 presents the DSC curves. In the temperature range evaluated for samples obtained at different milling times (20 and 50 min), two endothermic peaks are observed. The first one, at 66 °C, is attributed to the elimination of volatile residues [46], and the second one, at 276 °C, associated with processes related to graphite, since according to various studies, oxidation processes and vitreous graphite transitions occur between 170 and 300 °C [47, 48].

Different materials such as HfC, SiC, and Si, among others, have been employed as sintering aids to enhance TaC densification; however, WC has not been comprehensively studied in this regard. Kelly *et al* observed that the WC hinders grain growth, enhancing density and improving mechanical properties, particulary fracture strength [28]. Consequently, the incorporation of the WC through a HEBM process yields several benefits across different areas.

Furthermore, based on the results obtained from the different characterization techniques employed in this work, the TaC-WC powder resembles commercial TaC powder. However, it is important to emphasize that these results were achieved in 50 min of milling under environmental conditions.
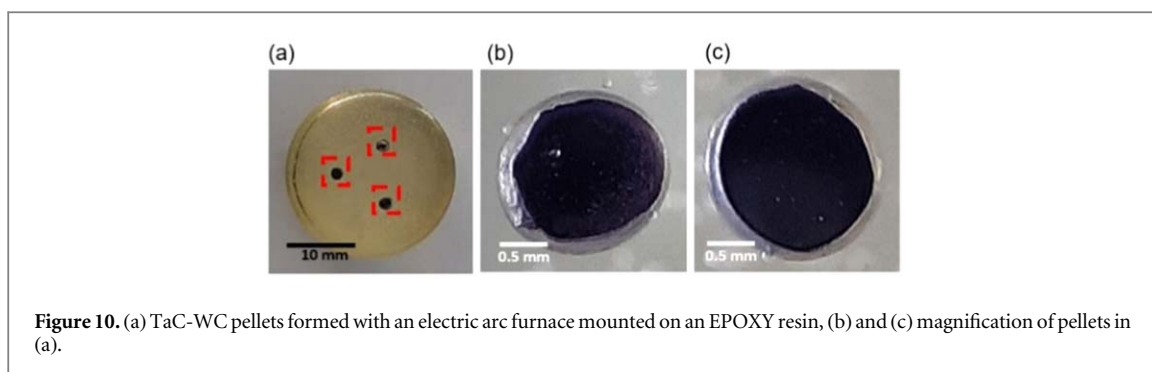
**Figure 10.** (a) TaC-WC pellets formed with an electric arc furnace mounted on an EPOXY resin, (b) and (c) magnification of pellets in (a).

### 3.2. TaC-WC consolidation via electric arc furnace

TaC-WC powders obtained by HEBM were consolidated using an electric arc furnace (EAF). Three pellets with semi-spherical shape were formed, with a thickness of approximately $1.5 \pm 0.1$ mm. The samples exhibited a density ($\rho$) of $14.7$ g cm$^{-3}$, with a relative density above 98%. TaC densification has been a challenge in recent years [21, 49], and several efforts have been made to enhance this property, involving the incorporation of sintering aids, along with the manipulation of pressure and temperature parameters throughout the sintering process [50, 51]. The combination of HEBM and electric arc furnace has achieved the densification of the TaC-WC in just a few minutes without the need to apply pressure.

The pellets were mounted on resin as shown in figure 10, and after solidification they were polished to achieve a homogeneous surface free of porosity and roughness for conducting a Vickers hardness test.

### 3.3. Characterization of TaC-WC after electric arc furnace and mechanical properties

XPS analysis was conducted to elucidate the surface chemical composition. Prior to running the XPS, a sputtering with Ar gas was performed for 360 s with an energy of 2 keV to remove impurities from the polished surface. XPS survey spectra revealed the presence of C, O, Ta, W, and Co, where the W and Co came from the milling material. No unexpected contaminant peaks were found (figure 11(a)). The elements identified via XPS are correlated with the results obtained by EDS. Peak attributions are found in table 3. C 1 s, O 1 s, Ta 4f and W 4f spectra are presented in figure 11. In figure 11(b), the C 1 s peaks at 283.3 are attributed to TaC and WC [52, 53], while 284.8 and 287.3 eV peaks are associated with C-C and O-C-O, respectively [54, 55]. The presence of C-C could be related with the HEBM, coming from raw material remnant, whilst the presence of O-C-O is ascribed to environmental pollutants. The O 1 s peaks are shown in figure 11(c).

Four peaks between 530.9–532.0 and in 533.5 were identified, corresponding to metals oxides (tantalum oxides) and O-C-O binding energies [56, 57]. Ta and W 4f core level spectra exhibit doublets of peaks in the binding energies 23.5 and 25.3, 24.5 and 26.4, 25.8 and 27.8, 27.2 and 29.3, 32.0 and 34.1 eV (figure 11(d)). The peaks at 23.5 and 25.3 are attributed to TaC [54], while the peaks at 32.0 and 34.1 are associated with WC [59]. The peaks at 27.2 and 29.3 eV ascribed to $Ta_2O_5$ [58], suggest that the sample presents an oxidation. It is important to mention that tantalum oxide is reduced by an argon ion beam to form a continuum of oxidation states. The peaks attribution at 24.5 and 26.4 and 25.8 and 27.6 eV correspond to these tantalum suboxides ($Ta_2O_3$ and $TaO_2$ respectively), caused by the sputtering process [58]. XPS results provide evidence that the sample surface consists mainly of TaC and WC, which is consistent with the x-ray analysis performed before the EAF treatment.

The XRD pattern of the TaC-WC pellets is shown in figure 12, revealing no changes in the TaC and WC crystalline phases. In addition, the presence of $TaO_2$ (space group $P4_2/mnm$) was identified. This finding aligns with the results obtained by XPS analysis, which discussed the formation of tantalum oxides during the EAF process. Moreover, the presence of $W_2C$ (space group $P\overline{3}1m$) and $W_3C_{0.375}$ (space group $Pm\overline{3}n$) in the sample was confirmed, indicating their formation during the heat treatment. It is important to note that the presence of these two phases was not detected by XPS, this can be attributed to the analyzed area. Nevertheless, despite the formation of tantalum oxides, $W_2C$ and $W_3C_{0.375}$ phases, the TaC structure remains unchanged. A slight shift observed in the peaks at larger angles which is associated to the spherical shape of the sample, as there is a height difference that interferes with the measurement. Furthermore, the diffractogram exhibited preferred orientation due to the nature of the bulk material, which is related to a higher frequency of occurrence as well as a variation in the intensity of the reflections of certain crystallographic planes.

Vickers hardness test was performed at different loads (0.49, 0.98, 2.94, 4.9 and 9.8 N) with a dwell time of 15 s. Five indentations per load were executed to obtain the average hardness and standard deviation. The graphical representation in figure 13 demonstrates that the hardness decreases as the load increases. This is
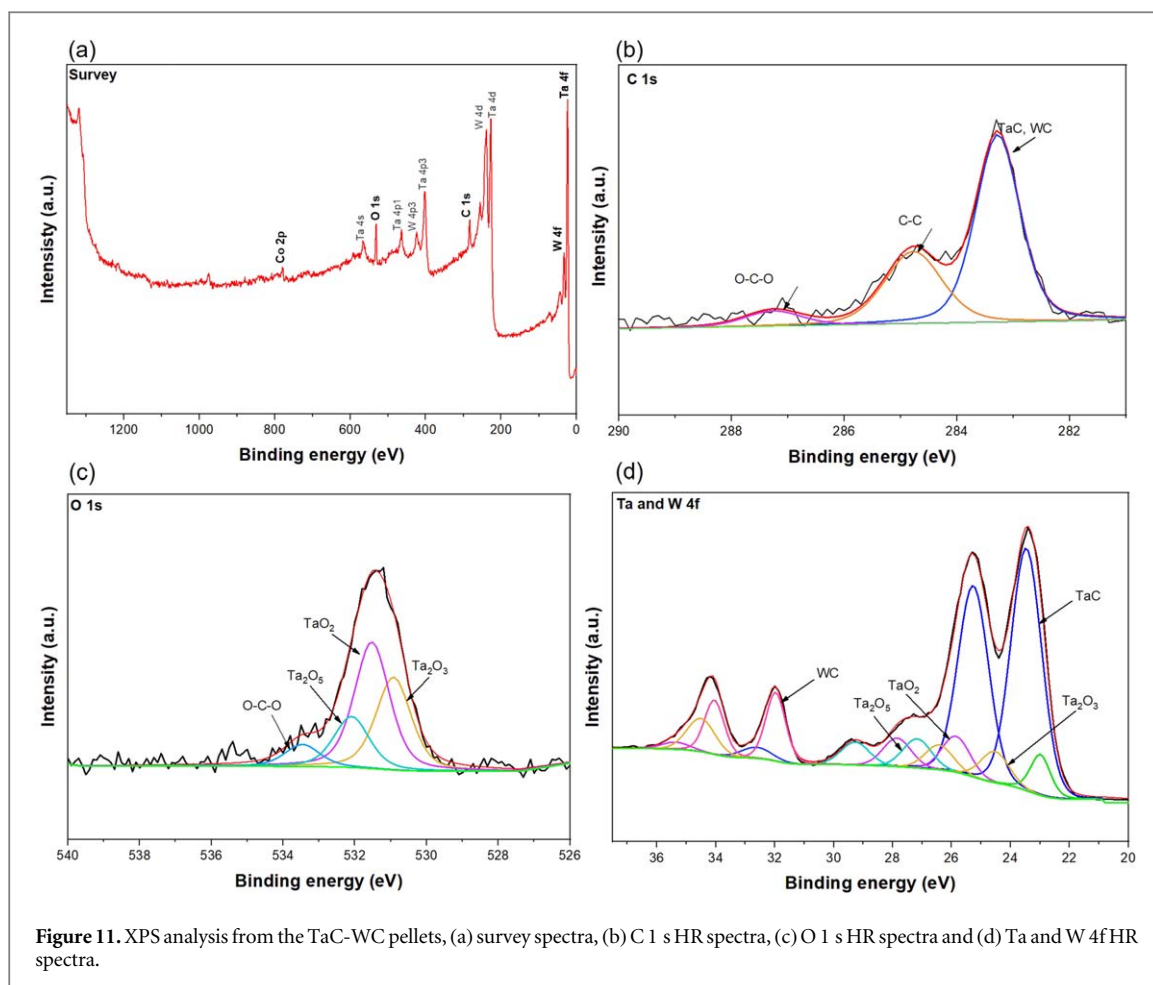
**Figure 11.** XPS analysis from the TaC-WC pellets, (a) survey spectra, (b) C 1 s HR spectra, (c) O 1 s HR spectra and (d) Ta and W 4f HR spectra.
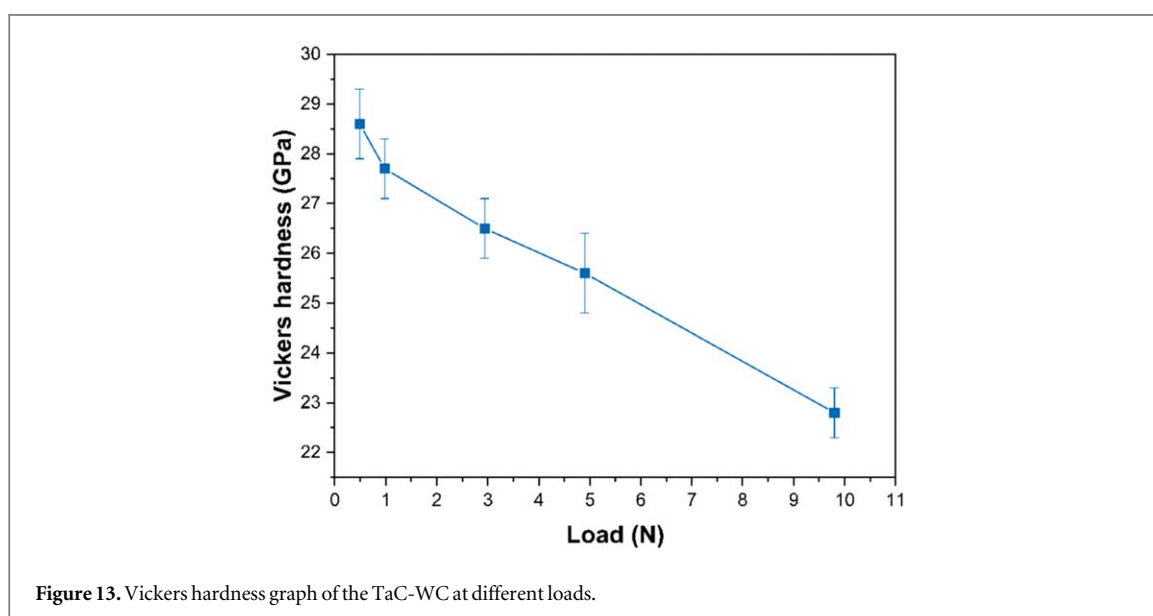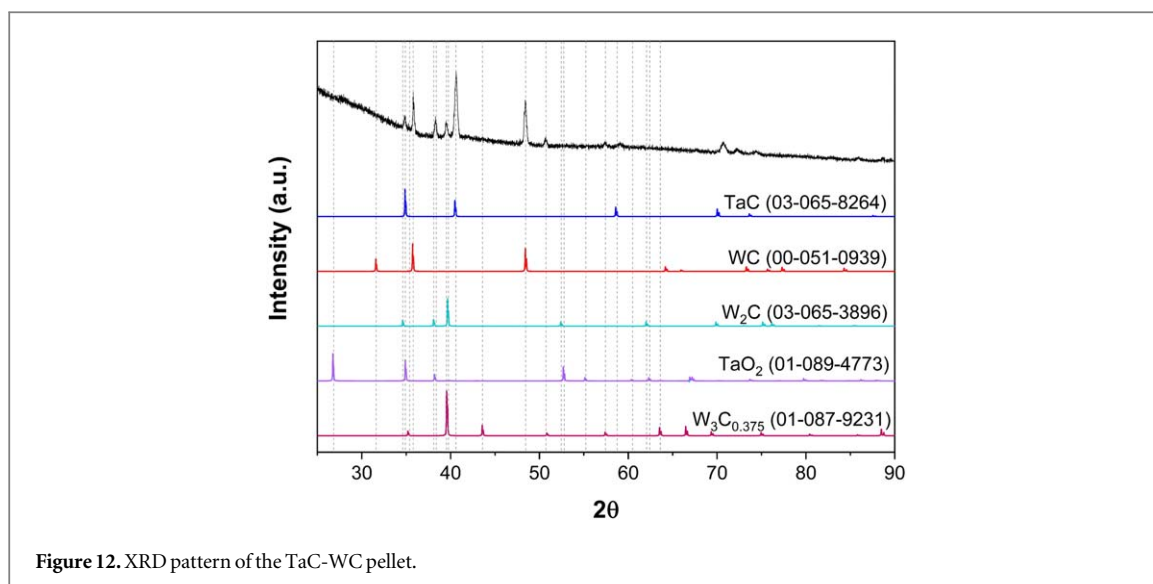
**Table 3.** Summary of XPS deconvolution.

| Suggested attribution | Binding energy (eV) | | References |
|---|---|---|---|
| C- (carbides TaC, WC) | 283.3 | | [52, 53] |
| C-C | 284.8 | | [54] |
| O-C-O | 287.3 | | [55] |
| O- (metals oxides Ta$_2$O$_3$, TaO$_2$, Ta$_2$O$_5$) | 530.9–532.0 | | [56] |
| O-C-O | 533.5 | | [57] |
| | Ta and W 4f7/2 | Ta and W 4f5/2 | |
| Ta-C | 23.5 | 25.3 | [54] |
| Ta-O (Ta$_2$O$_3$) | 24.5 | 26.4 | [58] |
| Ta-O (TaO$_2$) | 25.8 | 27.8 | [58] |
| Ta-O (Ta$_2$O$_5$) | 27.2 | 29.3 | [58] |
| W-C | 32.0 | 34.1 | [59] |

known as normal Indentation Size Effect (ISE) and has been observed in different materials such as diamond and some ceramics [32].

According to the results obtained in the microhardness category with a load of 0.49 N, the sample has a hardness of $28.6 \pm 0.7$ GPa, whilst at 0.98 N the material presents a hardness of $27.7 \pm 0.6$ GPa. On the other hand, in the low load category with a load of 4.9 N, the sample has a hardness of $25.6 \pm 0.8$ GPa, and at 9.8 N the hardness is $22.8 \pm 0.5$ GPa. Therefore, the material is classified as a hard material (Vickers hardness $\geqslant 10$ GPa) [60].

TaC hardness is correlated with various parameters, including crystalline structure, grain size, density, porosity and chemical bonds [27].

Silvestroni *et al* employed mechanical milling for 24 h, followed by a heat treatment in a furnace at 1400 °C under a vacuum <5 Pa for 30 min to sinter TaC, resulting in a hardness of $11.14 \pm 0.77$ GPa at an applied load of
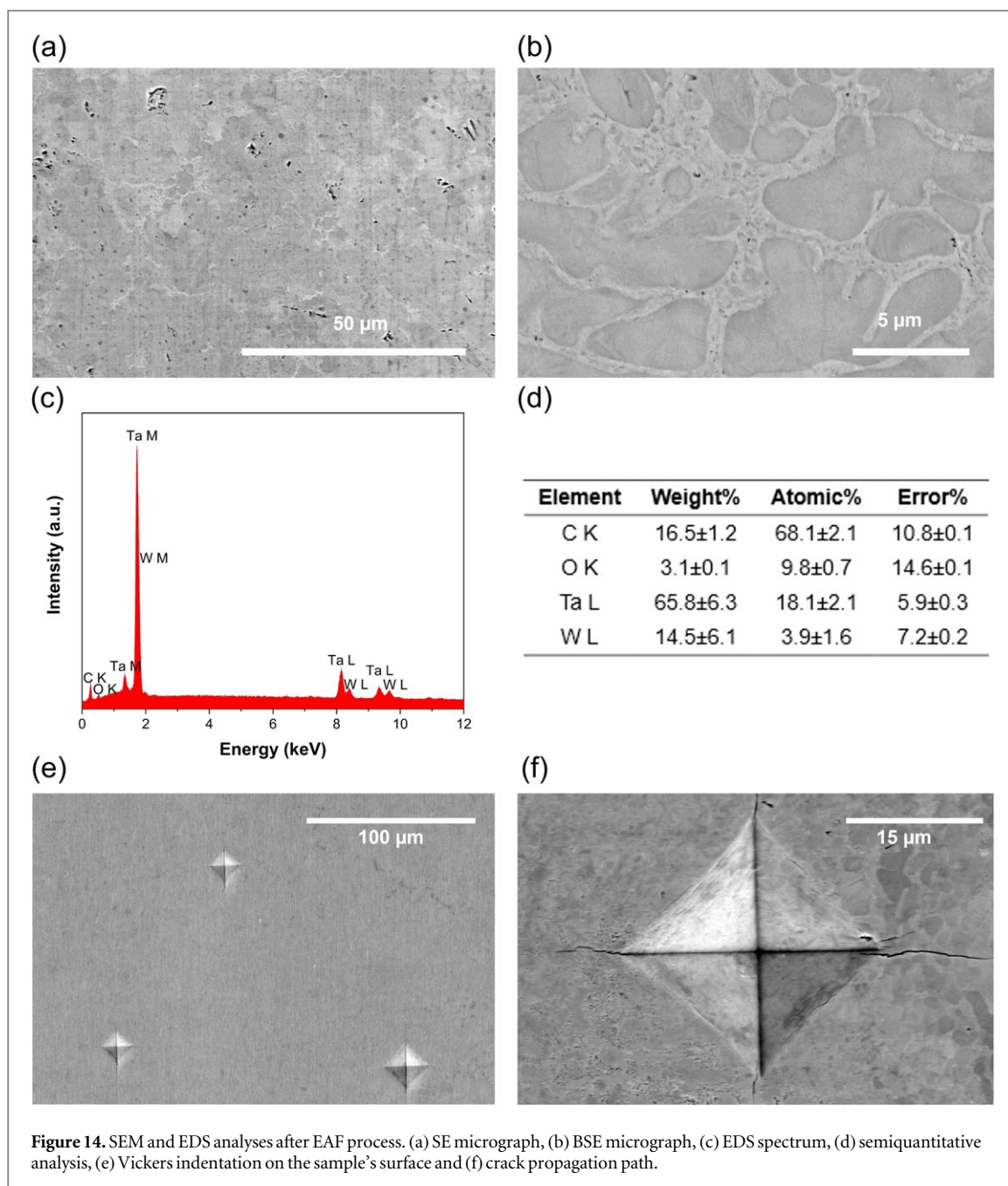
**Figure 12.** XRD pattern of the TaC-WC pellet.



**Figure 13.** Vickers hardness graph of the TaC-WC at different loads.

9.8 N, and with the incorporation of $5MoSi_2$ as a sintering aid, the hardness increased to $13.69 \pm 0.35$ GPa [61]. Zhang *et al* sintered TaC-$B_4C$ by HP at 2100 °C with a Vickers hardness of $16.3 \pm 0.2$ GPa under an applied load of 4.9 N and a dwell time of 15 s [1]. Sun *et al* sintered TaC through the high-pressure and high-temperature sintering method at 5.5 GPa and 1400 °C, obtaining a microhardness of 28.2 GPa under an applied load of 0.98 N [22]. Comparing the results presented in the present work with those obtained through alternative synthesis and sintering methods involving high pressures and temperatures, the hardness of the samples after EAF treatment are significantly higher than values reported in the literature.

WC presence in the TaC samples is attributed to the synthesis process resulting from ball milling materials. In accordance with different studies, the addition of TMC as sintering aid enhances their hardness and densification [1, 17]. Furthermore, Granados-Fitch *et al* reported that WC also improves catalysis properties [13], meaning that it is a beneficial addition in many fields.

Figure 14 presents the SEM micrographs of the TaC-WC samples after EAF. Figure 14(a) shows the surface of the sample, which exhibits pores of different sizes. Upon magnifying the image, the pores become more discernible, and there is an evident contrast attributed to the various phases in the sample (figure 14(b)). The EDS analysis shown in figure 14(c) indicates the presence of Ta, W, C and O. According to the semi-quantitative study, the wt% obtained for each element are related to those acquired by the Rietveld refinement before EAF treatment.

The presence of impurities in the samples, originating from the synthesis and consolidation processes, can potentially influence an increase in the oxygen content, resulting in the formation of pores within the material's

**Figure 14.** SEM and EDS analyses after EAF process. (a) SE micrograph, (b) BSE micrograph, (c) EDS spectrum, (d) semiquantitative analysis, (e) Vickers indentation on the sample's surface and (f) crack propagation path.

microstructure [62, 63]. However, despite the pore formation, the hardness of the material was not compromised.

Figure 14(e) exhibits the Vickers indentation on the surface of the samples. According to the measurements conducted, these Vickers indentations correspond to applied loads of 4.9 and 9.8 N. Figure 14(f) presents the crack propagation path originating from the Vickers corners, revealing a linear trajectory of crack propagation.

Young modulus was determined using the pore volume calculated by BET for TaC powders. Vickers hardness, Young's modulus and fracture toughness of the TaC-WC materials were 22.8 GPa, 535.9 GPa and 6.6 MPa m$^{1/2}$, respectively. Table 4 presents the values obtained in this study in comparison to those reported in literature. Zhang *et al* sintered TaC- 50 vol% HfC via SPS at 1850 °C under 60 MPa for 10 min, achieving a relative density above 98% and Vickers hardness, Young's modulus and fracture toughness values of 17.15 GPa, 523.83 GPa and 6.03 MPa m$^{1/2}$, respectively [38]. Cedillos-Barraza *et al* consolidated TaC-HfC with a relative density above 95% using SPS at 2450 °C. The resulting Vickers hardness, Young's modulus and fracture toughness were 20.4 GPa, 549 GPa and 2.9 MPa m$^{1/2}$, respectively [17]. Liu *et al* sintered TaC by SPS at 1800 °C under 80 MPa for 10 min, enhancing a density above 97% and a Vickers hardness, Young's modulus and fracture toughness of 15.60 GPa, 512.66 GPa and 3.59 MPa m$^{1/2}$, respectively [64].

**Table 4.** Density and mechanical properties of TaC-WC in comparison to values reported in literature.

| Material | Relative density % | Vickers hardness Hv at 9.8 N (GPa) | Young's modulus E (GPa) | Fracture toughness (MPa m$^{1/2}$) | References |
|---|---|---|---|---|---|
| TaC-WC | ~98% | 22.8 | 535.9 | 6.6 | * |
| TaC-HfC | ~98% | 17.15 | 523.82 | 6.03 | [38] |
| TaC-HfC | ~95% | 20.4 | 549 | 2.9 | [17] |
| TaC | ~97% | 15.6 | 512.66 | 3.59 | [64] |

*Relative density and mechanical properties obtained in the present work.

Our findings suggest that TaC-WC can be obtained within minutes by combining HEBM for 50 min under environmental conditions and using an EAF. This pioneering approach enables the production of dense materials with mechanical properties suitable for UHTCs while reducing production costs due to the synthesis conditions and shortened manufacturing time. Nevertheless, ongoing investigations will focus on studying the microstructure of the material to elucidate the relationship between grain size and mechanical properties.

## 4. Conclusions

This study emphasizes the synthesis of TaC-WC powders in 50 min under environmental conditions. High-energy ball milling facilitates the material formation, and particle size reduction, as well as the incorporation of WC as sintering aid, which enhances both densification and mechanical properties. The consolidation of the material through an electric arc furnace was accomplished in just a few minutes without applying pressure and yields samples with relative densities exceeding 98%. The emergence of tantalum oxides during the sintering process is attributed to impurities in the raw materials; however, this occurrence does not compromise material density or induce significant porosity. Furthermore, XRD analysis after electric arc furnace confirms the consistency of TaC and WC phases. Vickers hardness of the TaC-WC at 9.8 N of load is $22.8 \pm 0.5$ GPa, while Young's modulus and fracture toughness measure 535.9 GPa and 6.6 M P a m $^{1/2}$, respectively. Notably, the mechanical properties after heat treatment exhibit a significant increase compared to values reported in the literature, showcasing promising potential applications in the ultra-high temperature ceramics industry. The combination of these two techniques for TaC-WC synthesis represents a novel approach, as this work is pioneering in the field. The findings highlight the attainment of a material characterized by high density, hardness, elastic modulus, and fracture toughness, all achieved while reducing synthesis and sintering times, which translates into significant cost savings.

## Acknowledgments

## Data availability statement

All data that support the findings of this study are included within the article (and any supplementary files).

## Credit

**A Vázquez-Pelayo:** Methodology, Validation, Investigation, Writing - Original Draft. **T Garcia-Mendoza:** Conceptualization, Methodology, Investigation. **I G Becerril-Juarez:** Methodology, Writing—Review & Editing. **E A Juarez-Arellano:** Writing—Review & Editing. **L K Mireles:** Writing—Review & Editing. **M Avalos-Borja:** Writing—Review & Editing, Supervision, Project Administration.

## ORCID iDs

A Vázquez-Pelayo ⬤ https://orcid.org/0000-0003-0852-758X
E A Juarez-Arellano ⬤ https://orcid.org/0000-0003-4844-8317
M Avalos-Borja ⬤ https://orcid.org/0000-0003-4515-6415

## References

[1] Zhang X, Hilmas G E and Fahrenholtz W G 2009 Densification and mechanical properties of TaC-based ceramics *Mater. Sci. Eng.* A **501** 37–43

[2] Nino A, Hirabara T, Sugiyama S and Taimatsu H 2015 Preparation and characterization of tantalum carbide (TaC) ceramics *Int. J. Refract. Met. Hard Mater.* **52** 203–8

[3] Jiang J, Wang S, Li W and Chen Z 2016 Low-temperature synthesis of tantalum carbide by facile one-pot reaction *Ceram. Int.* **42** 7118–24

[4] Fahrenholtz W G and Hilmas G E 2017 Ultra-high temperature ceramics: materials for extreme environments *Scr. Mater.* **129** 94–9

[5] López-De-La-Torre L, Winkler B, Schreuer J, Knorr K and Avalos-Borja M 2005 Elastic properties of tantalum carbide (TaC) *Solid State Commun.* **134** 245–50

[6] Zhang X, Hilmas G E and Fahrenholtz W G 2008 Densification, mechanical properties, and oxidation resistance of TaC-TaB2 ceramics *J. Am. Ceram. Soc.* **91** 4129–32

[7] Ni D *et al* 2022 Advances in ultra-high temperature ceramics, composites, and coatings *J. Adv. Ceram.* **11** 1–56

[8] Chan J Y and Kauzlarich S M 1997 Rare-earth halides as fluxes for the synthesis of tantalum and niobium carbide *Chem. Mater.* **9** 531–4

[9] Wang L, Zhang F, Dai W, Cheng Q, Lu L, Zhang K, Lin M, Shen M and Wang D 2019 One step transformation of waste polyvinyl chloride to tantalum carbide@carbon nanocomposite at low temperature *J. Am. Ceram. Soc.* **102** 6455–62

[10] Li P G, Lei M, Sun Z B, Cao L Z, Guo Y F, Guo X and Tang W H 2007 C3N4 as a precursor for the synthesis of NbC, TaC and WC nanoparticles *J. Alloys Compd.* **430** 237–40

[11] Liu C, Wang W, He Q, Wang A, Wu J, Wang H, Zhang J and Fu Z 2018 Synthesis of ultra-fine tantalum carbide powders by a combinational method of sol–gel and spark plasma sintering *Ceram. Int.* **44** 19106–12

[12] Sevast'yanov V G, Simonenko E P, Ignatov N A, Ezhov Y S and Kuznetsov N T 2010 Low-temperature synthesis of TaC through transparent tantalum-carbon containing gel *Inorg. Mater.* **46** 495–500

[13] Granados-Fitch M G, Juarez-Arellano E A, Quintana-Melgoza J M and Avalos-Borja M 2016 Mechanosynthesis of rhenium carbide at ambient pressure and temperature *Int. J. Refract. Met. Hard Mater.* **55** 11–5

[14] Wollmershauser J A, Feigelson B N, Gorzkowski E P, Ellis C T, Goswami R, Qadri S B, Tischler J G, Kub F J and Everett R K 2014 An extended hardness limit in bulk nanoceramics *Acta Mater.* **69** 9–16

[15] Chrzanowska J, Kurpaska L, Giżyński M, Hoffman J, Szymański Z and Mościcki T 2016 Fabrication and characterization of superhard tungsten boride layers deposited by radio frequency magnetron sputtering *Ceram. Int.* **42** 12221–30

[16] Garcia-Mendoza T, Martinez-Garcia A, Becerril-Juarez I G, Lopez-Vazquez E, Avalos-Borja M, Valera-Zaragoza M and Juarez-Arellano E A 2020 Mechanosynthesis of metastable cubic δ-Ta1−xN *Ceram. Int.* **46** 23049–58

[17] Cedillos-Barraza O, Grasso S, Nasiri N A, Jayaseelan D D, Reece M J and Lee W E 2016 Sintering behaviour, solid solution formation and characterisation of TaC, HfC and TaC-HfC fabricated by spark plasma sintering *J. Eur. Ceram. Soc.* **36** 1539–48

[18] Manotas-Albor M, Vargas-Uscategui A, Palma R and Mosquera E 2014 *In situ* production of tantalum carbide nanodispersoids in a copper matrix by reactive milling and hot extrusion *J. Alloys Compd.* **598** 126–32

[19] Liu L, Geng G, Jiang Y, Wang Y, Hai W, Sun W, Chen Y and Wu L 2017 Microstructure and mechanical properties of tantalum carbide ceramics: Effects of Si3N4 as sintering aid *Ceram. Int.* **43** 5136–44

[20] Li S, Wei C, Cheng J, Zhang L, Gao P, Wang P, Zhou L and Wen G 2020 Crack tolerant TaC–SiC ceramics prepared by spark plasma sintering *Ceram. Int.* **46** 25230–5

[21] Zhang X, Hilmas G E, Fahrenholtz W G and Deason D M 2007 Hot pressing of tantalum carbide with and without sintering additives *J. Am. Ceram. Soc.* **90** 393–401

[22] Sun W, Kuang X, Liang H, Xia X, Zhang Z, Lu C and Hermann A 2020 Mechanical properties of tantalum carbide from high-pressure/high-Temperature synthesis and first-principles calculations *Phys. Chem. Chem. Phys.* **22** 5018–23

[23] Bakshi S R, Musaramthota V, Lahiri D, Singh V, Seal S and Agarwal A 2011 Spark plasma sintered tantalum carbide: Effect of pressure and nano-boron carbide addition on microstructure and mechanical properties *Mater. Sci. Eng.* A **528** 1287–95

[24] Neuman E W, Hilmas G E and Fahrenholtz W G 2022 Pressureless sintering of zirconium diboride with carbon and boron carbide nanopowder *Ceram. Int.* **48** 13071–9

[25] Granados-Fitch M G, Quintana-Melgoza J M, Juarez-Arellano E A and Avalos-Borja M 2021 Rhenium borides (Re3B and ReB2) mechanosynthesis and their use as a catalyst for H2 production from biomass pyrolysis *Mater. Res. Bull.* **137** 111180

[26] Zhang S C, Hilmas G E and Fahrenholtz W G 2006 Pressureless densification of zirconium diboride with boron carbide additions *J. Am. Ceram. Soc.* **89** 1544–50

[27] Chang L, Jiang Y, Wang W, Yue X and Ru H 2019 Ultrafine WC-0.5Co-xTaC cemented carbides prepared by spark plasma sintering *Int. J. Refract. Met. Hard Mater.* **84** 104994

[28] Kelly J P, Vakharia V S, Novitskaya E and Graeve O A 2022 Densification and fracture responses of (Ta1−xWx)C–WC composites *Adv. Eng. Mater.* **24** 1–9

[29] Degen T, Sadki M, Bron E, König U and Nénert G 2014 The HighScore suite *Powder Diffr.* **29** S13–8

[30] Kilaas R 2013 MacTempasX computer program

[31] ASTM E384 - 17 2017 Standard test method for microindentation hardness of materials *ASTM Int.* **03.01** 40

[32] Shahdad S A, McCabe J F, Bull S, Rusby S and Wassell R W 2007 Hardness measured with traditional Vickers and Martens hardness methods *Dent. Mater.* **23** 1079–85

[33] Chuenarrom C, Benjakul P and Daosodsai P 2009 Effect of indentation load and time on knoop and vickers microhardness tests for enamel and dentin *Mater. Res.* **12** 473

[34] Nielsen L F 1984 Elasticity and damping of porous materials and impregnated materials *J. Am. Ceram. Soc.* **67** 93–8

[35] Toth L 2014 *Transition Metal Carbides and Nitrides* (Elsevier Science)

[36] Anstis G R, Chantikul P, Lawn B R and Marshall D B 1981 A critical evaluation of indentation techniques for measuring fracture toughness: I, direct crack measurements *J. Am. Ceram. Soc.* **64** 533–8

[37] Demirskyi D, Nishimura T, Suzuki T S, Yoshimi K and Vasylkiv O 2022 Consolidation and high-temperature properties of ceramics in the TaC–NbC system *J. Am. Ceram. Soc.* **105** 7567–81

[38] Zhang C, Gupta A, Seal S, Boesl B and Agarwal A 2017 Solid solution synthesis of tantalum carbide-hafnium carbide by spark plasma sintering *J. Am. Ceram. Soc.* **100** 1853–62

[39] Kim T and Wooldridge M S 2001 Catalytically assisted self-propagating high-temperature synthesis of tantalum carbide powders *J. Am. Ceram. Soc.* **84** 976–82

[40] Al-Habib D S H, Balak Z and Asl M S 2022 Spark plasma sinterability of TaC-based composites co-doped with SiC, TiC and graphene *Diam. Relat. Mater.* **130** 109496

[41] Song B, Zhang L and Shi Y 2023 *Microlattice Metamaterials* (Elsevier Inc)

[42] Nisar A, Ariharan S and Balani K 2018 Densification kinetics and mechanical properties of tantalum carbide *Int. J. Refract. Met. Hard Mater.* **73** 221–30

[43] Liu J X, Kan Y M and Zhang G J 2010 Pressureless sintering of tantalum carbide ceramics without additives *J. Am. Ceram. Soc.* **93** 370

[44] Thommes M, Kaneko K, Neimark A V, Olivier J P, Rodriguez-Reinoso F, Rouquerol J and Sing K S W 2015 Physisorption of gases, with special reference to the evaluation of surface area and pore size distribution (IUPAC Technical Report) *Pure Appl. Chem.* **87** 1051–69

[45] Sing K S W 1995 Physisorption of nitrogen by porous materials *J. Porous Mater.* **2** 5–8

[46] Carvajal-Campos Y, Ceballos-Mendivil L, Baldenebro-López F, Pérez-Rábago C and Estrada C A 2019 Synthesis and characterization of tantalum carbide nanoparticles using concentrated solar energy *Adv. Powder Technol.* **30** 2574–9

[47] Fryczkowski R, Gorczowska M, Ślusarczyk C, Fryczkowska B and Janicki J 2013 The possibility of obtaining graphene/polymer composites from graphene oxide by a one step process *Compos. Sci. Technol.* **80** 87–92

[48] Liou Y J and Huang W J 2014 High temperature phase transitions of graphene oxide paper from graphite oxide solution *J. Mater. Sci. Technol.* **30** 1088–91

[49] Rezaei F, Kakroudi M G, Shahedifar V, Vafa N P and Golrokhsari M 2017 Densification, microstructure and mechanical properties of hot pressed tantalum carbide *Ceram. Int.* **43** 3489–94

[50] Liu L, Ye F and Zhou Y 2011 New route to densify tantalum carbide at 1400 °C by spark plasma sintering *Mater. Sci. Eng.* A **528** 4710–4

[51] Liu H, Liu L, Ye F, Zhang Z and Zhou Y 2012 Microstructure and mechanical properties of the spark plasma sintered TaC/SiC composites: effects of sintering temperatures *J. Eur. Ceram. Soc.* **32** 3617–25

[52] Di C, Yan X, Yang Y, Ye W, Zhao M and Li D 2021 Wear behaviors and high-temperature oxidation resistance properties of tantalum carbide layer *Ceram. Int.* **47** 32766–74

[53] Krasovskii P V, Malinovskaya O S, Samokhin A V, Blagoveshchenskiy Y V, Kazakov V A and Ashmarin A A 2015 XPS study of surface chemistry of tungsten carbides nanopowdersproduced through DC thermal plasma/hydrogen annealing process *Appl. Surf. Sci.* **339** 46–54

[54] Zhu Y, Dong M, Mao F, Guo W, Li J and Wang L 2021 Self-adaption Ta/TaC multilayer coating with fine grains: toward excellent corrosion resistance in aggressive environment *J. Mater. Sci.* **56** 14298–313

[55] Gengenbach T R, Major G H, Linford M R and Easton C D 2021 Practical guides for x-ray photoelectron spectroscopy (XPS): Interpreting the carbon 1s spectrum *J. Vac. Sci. Technol.* A **39** 013204

[56] Moulder J F and Chastain J 1992 *Handbook of X-ray Photoelectron Spectroscopy: A Reference Book of Standard Spectra for Identification and Interpretation of XPS Data* (Physical Electronics Division, Perkin-Elmer Corporation)

[57] Beamson G and Briggs D 1992 High resolution XPS of organic polymers: the scienta ESCA300 database *J. Chem. Educ.* **70** A25

[58] Simpson R, White R G, Watts J F and Baker M A 2017 XPS investigation of monatomic and cluster argon ion sputtering of tantalum pentoxide *Appl. Surf. Sci.* **405** 79–87

[59] Abad M D, Muñoz-Márquez M A, El Mrabet S, Justo A and Sánchez-López J C 2010 Tailored synthesis of nanostructured WC/a-C coatings by dual magnetron sputtering *Surf. Coatings Technol.* **204** 3490–500

[60] Zhao Z, Xu B and Tian Y 2016 Recent advances in superhard materials *Annu. Rev. Mater. Res.* **46** 383

[61] Silvestroni L, Bellosi A, Melandri C, Sciti D, Liu J X and Zhang G J 2011 Microstructure and properties of HfC and TaC-based ceramics obtained by ultrafine powder *J. Eur. Ceram. Soc.* **31** 619–27

[62] Sciti D, Silvestroni L and Medri V 2014 Sintering and Densification Mechanisms of Ultra-High Temperature Ceramics *Ultra-High Temperature Ceramics: Materials for ExtremeEnvironment Applications* (Wiley) 112–143

[63] Baik S and Becher P F 1987 Effect of oxygen contamination on densification of TiB2 *J. Am. Ceram. Soc.* **70** 527–30

[64] Liu C, Wang A, Tian T, Hu L, Guo W, He Q, Xie J, Wang W, Wang H and Fu Z 2021 Sintering and densification mechanisms of tantalum carbide ceramics *J. Eur. Ceram. Soc.* **41** 7469–77